JOM, Vol. 72, No. 5, 2020
https://doi.org/10.1007/s11837-020-04105-8

Method for Fabricating Depth-Specific TEM In Situ Tensile Bars

P.H. WARREN,[1] G. WARREN,[1] M. DUBEY,[2,3] J. BURNS,[4] Y.Q. WU,[2,3] and J.P. WHARRY [1,5]

1.—Purdue University, 205 Gates Road, West Lafayette, IN 47906, USA. 2.—Boise State University, 1910 University Drive, Boise, ID 83725, USA. 3.—Center for Advanced Energy Studies, 995 MK Simpson Blvd, Idaho Falls, ID 83401, USA. 4.—Idaho National Laboratory, 1955 North Fremont Ave, Idaho Falls, ID 83415, USA. 5.—e-mail: jwharry@purdue.edu

The growing use of ion irradiation to assess degradation of nuclear materials has created a need to develop novel methods to probe the mechanical response of shallow ion-irradiated layers. Transmission electron microscopy (TEM) in situ mechanical testing can isolate the ion-irradiated layer from its unirradiated substrate. However, there is a lack of established procedures for preparing TEM in situ mechanical testing specimens from bulk materials requiring depth-specific examination, e.g., target dose on the ion irradiation damage profile. This study demonstrates a new method for extracting depth-specific TEM in situ tensile bars from a bulk specimen of Fe-5 wt.%Mo. Measured yield stress, ultimate tensile stress, Young's modulus, and elongation are consistent with those properties obtained from similarly sized Fe and Mo single-crystal nanowires. Results are discussed in the context of the specimen size effect.

INTRODUCTION

Ion irradiation is frequently used as a surrogate for neutron irradiation to evaluate the high-fluence degradation of cladding and structural alloys in advanced nuclear reactor concepts.[1–3] Many of the envisaged service conditions require these alloys to withstand damage doses of several hundreds of displacements per atom (dpa). Accumulating these doses in test reactors is challenging because of the relatively low fluence rates in addition to the limited availability and high cost of test reactor experiments. However, ions accelerate testing times and reduce costs by delivering fluence rates at least two orders of magnitude greater than that from fast neutrons. Moreover, ion-irradiated materials have little to no residual radioactivity. Hence, ion irradiation has been used for scoping studies that rapidly evaluate the relative performance of nuclear materials.

However, a limitation of ion irradiation is the shallow damage profile, typically on the order of a few hundreds of nm to a few μm. The irradiated microstructure can be readily observed in this near-surface region, using site-specific focused ion beam (FIB) milling of transmission electron microscopy (TEM) lamellae. Unfortunately, corresponding mechanical properties are more challenging to extract from this shallow ion-irradiated layer. In the last decade, significant advancements have been made in reducing the geometry of mechanical tests, to progressively move toward testing only the ion-irradiated layer. Among the most mature of these small-scale mechanical testing configurations is nanoindentation,[4] which has demonstrated efficacy for evaluating properties such as yield strength, elastic modulus, and strain-hardening coefficients of irradiated materials.[5–10] Oblique cross-sectional preparation of the ion-irradiated specimen has further advanced the resolution of nanoindentation.[11] Small-scale mechanical tests conducted in situ within a scanning electron microscope (SEM) have also been used extensively for understanding deformation behaviors[12–15] and quantitatively evaluating mechanical properties of irradiated materials.[16–19] However, SEM in situ mechanical tests are still unable to isolate the response of the ion-irradiated layer from the unirradiated substrate. Subsequently, TEM in situ mechanical testing has been demonstrated on ion-irradiated materials,[20–28] with the distinction of requiring electron-transparent specimens that are sufficiently small that the mechanical response of the ion-irradiated layer can be completely isolated

(Published online March 10, 2020)

from that of the unirradiated substrate. A distinct advantage of TEM in situ mechanical testing is the ability to gain fundamental insights into the deformation mechanisms and physical behavior of materials.[29,30]

TEM in situ mechanical testing has been demonstrated on a variety of ion-irradiated materials, using several different testing modes. Pillar compression tests have been used to evaluate the yield strength and elastic modulus on ion-irradiated Cu[31] and a ferrous oxide dispersion strengthened (ODS) alloy.[25] While pillars are relatively easy to fabricate and test, it is also easy to introduce taper during pillar fabrication, which causes uneven axial load distribution along the pillar.[32] Additionally, pillars can buckle during loading,[32] and a significant fraction of the applied load is transferred to the pillar base.[25,33] Many of these challenges, however, can be resolved using tensile testing. Tensile bars can be tested uniaxially, in which load is distributed homogeneously along the gauge section, and free of buckling.

TEM in situ tensile bars, however, are difficult to fabricate from an ion-irradiated layer. Most studies conducting TEM in situ tensile testing use nanowires, nanotubes, or freestanding thin films[34–37] that do not require further preparation. Of the studies that have used a focused ion beam (FIB) to shape TEM in situ tensile bars, many shape the bars from as-grown or as-deposited thin films or single crystals[35,36,38] or from electro-jet polished samples.[39] However, ion irradiations are usually conducted on a bulk specimen (rather than a thin film), and the $\sim \mu$m damage layer limits the ease of conducting electropolishing. These concerns, together with the more widespread access to higher-throughput FIB instruments (e.g., Xe plasma FIB), has pushed the need to develop a FIB-based method for extracting TEM in situ tensile specimens from near-surface ion-irradiated layers. Work from Morrow et al.[40] has used FIB to lift out a lamella planted onto a large dogbone utilized in a TEM straining holder. For depth-sensing TEM in situ mechanical testing holders, most FIB extracted tensile specimens use a gripper,[41] and those which use a push-to-pull tensile device[42] do not clearly describe the FIB fabrication process.

This article will present an efficient and reliable FIB method for creating TEM in situ tensile bars to be used in a push-to-pull device that specifically considers the challenges of working with ion-irradiated surface layers. However, the method is versatile and can be used on non-irradiated materials; proof of concept herein, in fact, is demonstrated on a non-irradiated Fe-5wt.% Mo alloy. This article will demonstrate that the method presented gives quantitative mechanical properties consistent with other small-scale mechanical tests.

METHODS

Materials

Specimens of a model Fe-5Mo (in wt.%) alloy were prepared by vacuum induction melting at Ames Laboratory. Solution annealing followed by water quenching produced a body-centered cubic (bcc) microstructure. The alloy was cut into 20 mm × 2 mm × 2 mm bars by electrical discharge machining (EDM). One of the 20 mm × 2 mm faces of a bar was polished using 1600 grit SiC paper and then with a 1-μm diamond suspension. Finally, the bar was vibratory polished for 3 h in colloidal silica. The composition was confirmed using an EDAX energy dispersive x-ray spectrometer (EDX) system on a FEI (now Thermo Fisher Scientific) Quanta 3D FEG SEM/FIB at the Center for Advanced Energy Studies (CAES).

Grain orientations of interest—from which TEM in situ tensile bars would be extracted—were identified using SEM-based grain orientation mapping on the prepared sample surface. An EDAX electron backscatter diffraction (EBSD) system on the same FEI Quanta 3D FEG SEM/FIB at CAES was used to map grain orientations. Because the initial intention was to conduct TEM in situ tensile testing in bright-field imaging mode, the [001] grain orientation has the optimal dislocation contrast in TEM bright field. However, a grain oriented along the $[\bar{1}13]$ direction was chosen because it was the closest available orientation to [001] on the mapped area.

Tensile Specimen Preparation

Site-specific focused ion beam (FIB) milling was done on the selected grain using a variation of the lift-out method[43] on the same FEI Quanta 3D FEG SEM/FIB dual beam at CAES. Two Pt guide bars, spaced 4 μm apart, with dimensions 10 μm × 0.5 μm × 1 μm, were first deposited at a current of 0.1 nA (Fig. 1a). These Pt guide bars served as an outline of the lamella that would later be extracted. Subsequently, two 10 μm × 8 μm × 4 μm trenches were milled adjacent to the lamella, using a beam current of 3 nA and an accelerating voltage of 30 kV. The Pt guide bars were not removed during the trenching step. However, after trenching, 0.3 nA cleaning cuts on both sides of the lamella were made, which completely removed the Pt guide bars (Fig. 1b). The lamella was freed from the bulk using "U"-cuts at 3 nA, after which the lamella was attached to a micro-manipulator needle and lifted out from the bulk specimen (Fig. 1c). At this point, the lamella dimensions were approximately 8 μm (width) × 6 μm (height) × 4 μm (thickness).

The lifted-out lamella was welded upright to the push-to-pull specimen mount (Fig. 1d). The $\sim$ 8 μm lamella width bridged the 2.5 μm gap on the push-to-pull device. The device was tilted in the FIB so as

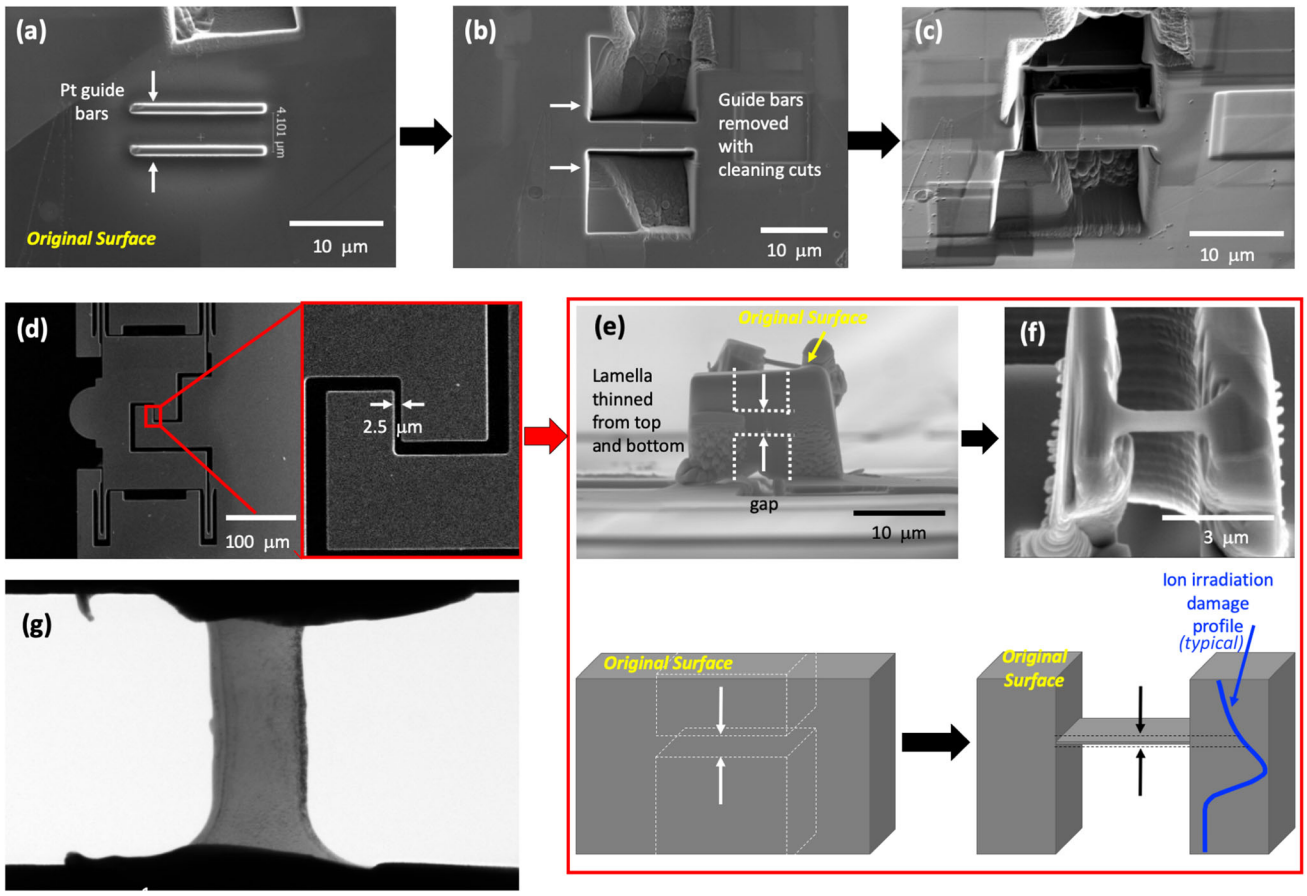

Fig. 1. Illustration of process for extracting and shaping TEM in situ tensile bars from bulk materials, beginning with (a) identification of region of interest, (b) FIB milling and (c) lift-out of bar, and (d) placement of lifted-out lamella onto push-to-pull device. The lamella then undergoes (e) final thinning to (f) specific depth of interest (which can correspond to a typical ion irradiation damage profile); also shown is (g) TEM image of final shaped and thinned tensile bar.

to view the lamella directly on one of the ~ 8 μm (width) $\times \sim 6$ μm (height) faces (Fig. 1e). Material was then removed using top-down and bottom-up milling until an electron-transparent region (which would later become the tensile beam) of ~ 100 nm thickness was produced (Fig. 1f). These milling steps were carried out at successively lower beam currents to minimize surface damage of the Ga beam,[44] much like the final thinning steps for a conventional TEM lamella. This top-down and bottom-up milling configuration also enabled targeting of a specific investigation depth, such as a depth corresponding to the desired fluence determined by the ion irradiation damage profile (Fig. 1e, f). Finally, the specimen was tilted to be head-on with the electron transparent region for final shaping of the tensile specimen. A gauge section was produced having dimensions of ~ 1.5 μm length and ~ 1 μm width; the thickness remained ≤ 100 nm (Fig. 1g). The final dimensions of each tensile bar are provided in Table I. The length and width were determined from bright-field micrographs collected from an FEI Tecnai G^2 TF30-FEG STwin STEM at CAES; the experimental error of these measurements is associated with the 0.2-nm resolution limit of the microscope. The thickness was determined using Gatan electron energy loss spectroscopy (EELS), which is known to have measurement error $\leq 10\%$.[45]

TEM in situ Tensile Testing

The TEM in situ tensile test was carried out in the aforementioned FEI Tecnai TF30-FEG STwin STEM at CAES operating at 300 kV and using a Hysitron (now Bruker) PI-95 Picoindenter fitted with a 20-μm diamond flat punch tip. Prior to application of mechanical load, the tensile bar was tilted to near the [001] zone axis for bright-field TEM imaging; TEM diffraction patterns were used to confirm the crystallographic orientation. Tensile testing was done in bright-field mode, continuously until failure, at a constant strain rate of 6×10^{-4} s^{-1}. The PI-95 has a displacement noise floor < 0.1 nm, which is the main contributor to error in measurements involving strain (e.g., modulus, strain rate, strain at failure), and a load noise floor < 0.2 μN, which is the main contributor to error in measurements involving stress (e.g., modulus, yield stress, ultimate tensile stress, stress at

Table I. Summary of experiment parameters and quantitative stress–strain results from two TEM in situ tensile bars tested

	Bar #1	Bar #2
Grain orientation	[$\bar{1}$13]	[$\bar{1}$13]
Length of gauge section (μm)	1.58	1.60
Width of gauge section (μm)	0.88	1.00
Thickness of gauge section (nm)	106 ± 10.6	135 ± 13.5
Cross-sectional area (μm^2)	0.094	0.135
Strain rate (s^{-1})	6.33×10^{-4} s^{-1}	6.25×10^{-4} s^{-1}
Yield strength (GPa)	1.40	1.56
Elastic modulus (GPa)	30.0	44.8
UTS (GPa)	1.9	2.0
Stress at failure (GPa)	1.92	2.02
Strain at failure (%)	7.1	4.6

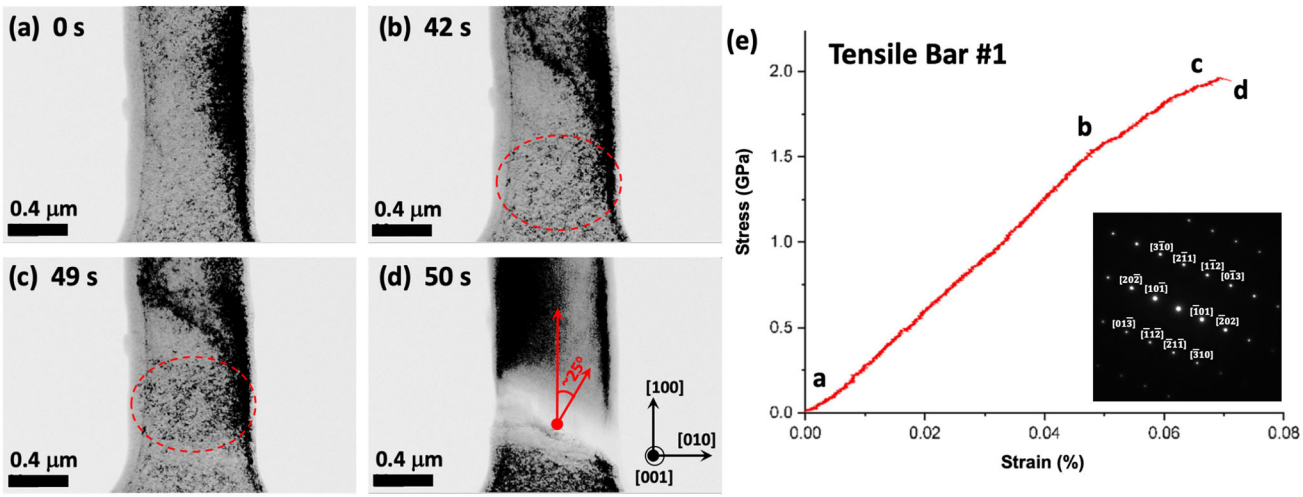

Fig. 2. TEM in situ tensile test #1, with still frames from (a) immediately before application of load, (b) yield, (c) immediately before fracture, and (d) fracture, each marked on the corresponding (e) stress–strain curve. Dislocation density increases are circled, and crystallographic orientations are shown as an inset in (d); confirmation by diffraction pattern is shown as an inset in (e).

failure). The TEM CCD output was continuously recorded as a video file at 30 frames per second (fps) and was stored using MJPEG compression.

After tensile fracture was achieved, the acquired load–displacement data were used to evaluate the additional load borne by the push-to-pull device spring, which was subtracted from the total applied load to obtain the load on the tensile bar. Two TEM in situ tensile bars were tested in this study for the purposes of replicability; the dimensions and loading parameters for these two bars are summarized in Table I.

RESULTS AND DISCUSSION

Observations from TEM In Situ Tensile Tests

Prior to application of any tensile load, the TEM in situ tensile bars contain a network of defects, shown as dark contrast in the bright-field TEM video still-frames (Figs. 2a and 3a). These defects are a combination of pre-existing dislocations in the alloy and FIB-induced damage. The tensile bars exhibit the propagation of bend contours during mechanical deformation (see still frames in Figs. 2b, c and 3b, c). Although the tensile bars are single crystals loaded uniaxially, the bend contours are believed to arise because of FIB-induced variations in the thickness and width of the gauge section, which produce fluctuations in load distribution and stress concentrations that appear as bend contours.

In the first specimen, plastic yield occurs coincident with an increase in dislocation density, at a real time of 42 s (circled region, Fig. 2b). This dislocation density continues to increase (Fig. 2c) in the region of the specimen where fracture eventually occurs. The fracture surface is oriented with an angle $\sim 25°$ between the fracture plane normal and the loading direction (Fig. 2d). The increase in dislocation activity near the fracture region may suggest that a dislocation-mediated deformation mechanism is active. However, the [100] grain orientation in bcc Fe is predicted to

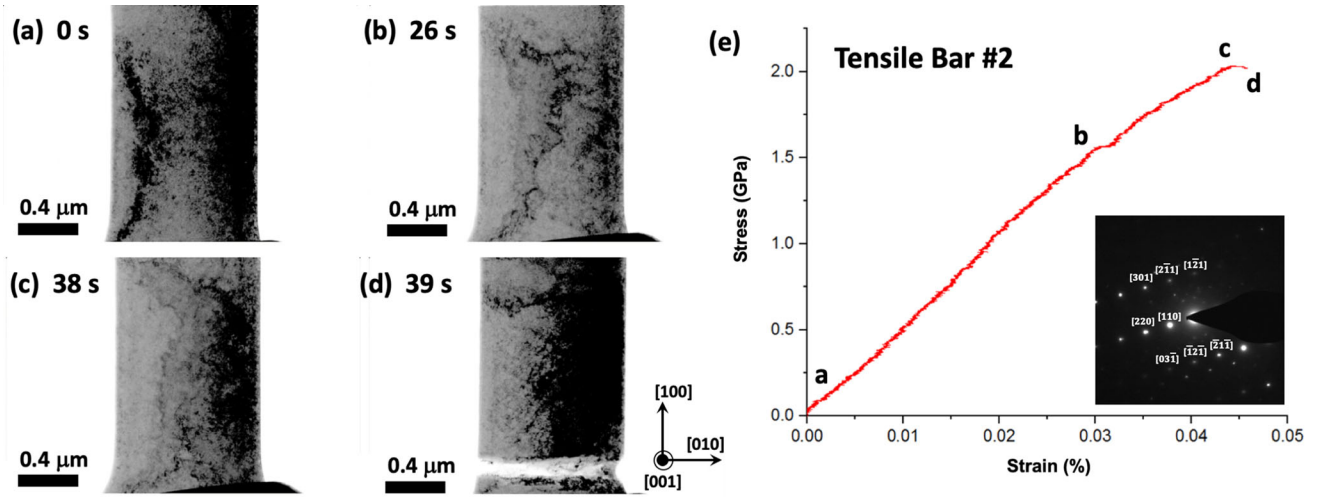

Fig. 3. TEM in situ tensile test #2, with still frames from (a) immediately before application of load, (b) yield, (c) immediately before fracture, and (d) fracture, each marked on the corresponding (e) stress–strain curve. Crystallographic orientations are shown as an inset in (d); confirmation by diffraction pattern is shown as an inset in (e).

deform through mechanical twinning.[46–48] Moreover, the most probable twinning plane is (112), the normal to which has a 24.1° angle to the loading direction in [100] bcc Fe nanowires[46,47]; this is consistent with the observed inclination of the fracture plane. Theoretical predictions of the critical twinning stress in α-Fe span a wide range of 0.43-7.12 GPa, depending upon the twinning mechanism, with experimental observations ~ 0.17 GPa.[49] Thus, it is plausible that the observed critical resolved shear stress (τ_{CRSS}) on the fracture plane, 1.01 GPa, is sufficiently high to induce mechanical twinning. However, the strain-hardening regime of the stress–strain curve does not exhibit any load drops or strain burst events that are typically indicative of mechanical twinning (Fig. 2e). There is also no TEM evidence of twinning in the tensile bar microstructure.

In the second specimen, there is no clear evidence of an increase in dislocation density during or after yielding, at the eventual site of fracture (Fig. 3b, c). However, the bend contouring in bright-field TEM may hinder clear discernment of dislocation and defect densities. The fracture surface occurs roughly along the [010] direction (Fig. 3d). Although no clear slip plane is obvious, the strain-hardening portion of the stress–strain curve (Fig. 3e) is indicative of dislocation glide, with no evidence of load drops due to mechanical twinning. Thus, deformation and fracture in the second specimen may be associated with dislocation motion introduced by the FIB damage, which is known to act as a source of dislocations.[38]

Assessing Mechanical Properties from TEM in situ Tensile Tests

The stress–strain curves obtained from the two demonstration tests are used to evaluate the yield stress, ultimate tensile stress (UTS), modulus of elasticity, and elongation (Table I). Despite the differences in the appearance of fracture surfaces between the two specimens, their measured yield stresses, UTS, and elastic moduli are consistent with one another, indicating replicability of the specimen fabrication process. The most notable difference between the two tests is the measured ductility at 7.1% elongation in the first specimen and 4.6% elongation in the second. However, these differences in ductility are to be expected given the larger τ_{CRSS} in the first specimen.

The average yield stress of the Fe-5Mo falls into close agreement with tensile yield stresses from SEM in situ tests of 100-nm-diameter Fe [101] single-crystal nanowires[13] and TEM in situ tests of 245-nm-diameter, 15% pre-strained Mo [001] nanofibers[50] (Fig. 4a). Compressive yield stresses from 100–200 nm diameter Fe [101] and [001] nanowires[13,51] and 370-nm-diameter pre-strained Mo [001] nanopillars[52] are also consistent with the Fe-5Mo yield stresses from this study, although compression-tension asymmetry typical of bcc metals and alloys is evident.[48] The nano-/microscale Fe, Mo, and Fe-5Mo yield strengths are all significantly larger than bulk Fe and Mo yield strengths, indicative of the specimen size effect.[32,53–60] The average UTS of the Fe-5Mo follows the same trends as the yield stress (Fig. 4b). That is, the Fe-5Mo falls into close agreement with UTS from single-crystal Fe and Mo SEM/TEM in situ tensile tests[13,50] as well as flow stress values from the corresponding single-crystal Fe and Mo SEM in situ compression tests.[13,51,52] Size effects are again pronounced in UTS values compared with bulk Fe and Mo.

These size effects in single, sub-micrometer sized crystals are understood to be caused by geometrical constraints on dislocation nucleation and motion,[56,61,62] which manifest as elevated yield stresses often referred to as the “smaller is

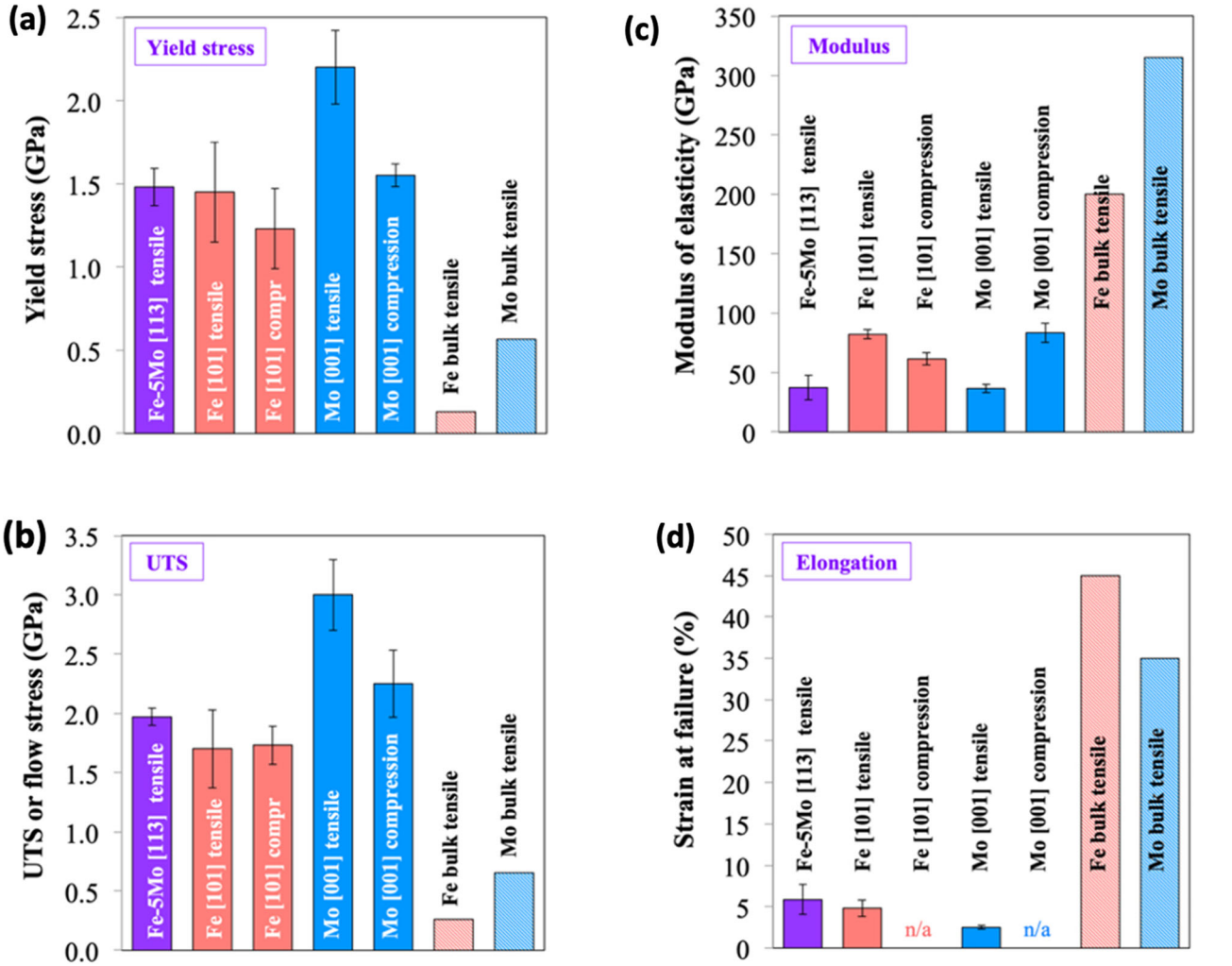

Fig. 4. (a) Yield stress, (b) UTS or flow stress, (c) elastic modulus, and (d) elongation of the Fe-5Mo [$\bar{1}$13] tensile bars in this study (violet bars), compared with Fe [101] nanowires (pink bars) tested in tension and compression,[13,51] Mo [001] nanowires (blue bars) tested in tension[50] and compression,[52] and bulk Fe and Mo (cross-hatched bars)[68] (Color figure online).

stronger" principle. Additionally, dislocations that nucleate in nanoscale specimens can more readily escape to the surface when the specimens are subject to low strain rates.[63,64] This dislocation starvation further exacerbates size effects in specimens such as those presented herein.[63,65] Nevertheless, the demonstrated TEM in situ tensile bar fabrication method can effectively create specimens that exhibit comparable a stress response as similarly sized single crystals of similar bcc metals.

The modulus of elasticity of the Fe-5Mo is comparable to moduli calculated from stress–strain curves of the same Fe and Mo single-crystal pillars and nanowires previously referenced from the archival literature[13,50–52] (Fig. 4c). All of these nano-/microscale specimens exhibit elastic moduli as much as an order of magnitude smaller than the elastic moduli for bulk Fe and Mo. However, it has been well established that moduli measured in small-scale tests are generally markedly low because a significant fraction of the applied stress is transferred away from the region of observation (e.g., the electron transparent region of the tensile bars in this study) and is borne by other portions of the test setup.[33] For example, finite element models (FEM) of TEM in situ compression pillars have shown much of the applied load is transferred from the pillars to the pillar base, resulting in low elastic moduli of the pillars.[25] It is plausible that similar stress transfer from the observation area, and into the ends of the lamella and the Pt weld regions, could explain the low measured modulus values. Surface atom decohesion leading to a low surface modulus has also been used to explain the low stochastic Young's modulus in nanowires and other miniaturized specimens having a high surface area-to-volume ratio.[66]

The $\sim$ 5% elongation observed in the Fe-5Mo is statistically consistent with the observations of $<$ 5% and $\sim$ 2.5% elongation in [101] Fe and [001] Mo nanowires tested in tension, respectively.[13,50] The ductility of nanoscopic, single-crystal specimens is an

order of magnitude lower than that of their bulk polycrystalline counterparts (Fig. 4d). This limited ductility is a size effect from the geometrical constraints on dislocation sources and mobility. Dislocation avalanches are typically observed in micrometer- and sub-micrometer-sized specimens, causing limited ductility and thus inhibiting plastic formability.[67] Surface atom decohesion can also reduce ductility in samples with a high surface area-to-volume ratio.[66] Plastic instability that arises when tensile samples do not satisfy the plane strain condition ($w/t \gg 1$ where w = width and t = thickness) can also reduce the measured elongation.[67]

CONCLUSION

A new method has been developed to extract TEM in situ tensile bars from a bulk specimen, with the ability to examine deformation at a depth of interest corresponding to, say, a specific depth on the ion irradiation damage profile. This method has been demonstrated on $[\bar{1}13]$ oriented bcc Fe-5Mo. In the real-time TEM videos, strain hardening has been observed coincident with dislocation-mediated deformation. The quantitative mechanical response is consistent with similarly sized Fe and Mo single-crystal nanowires and nanofibers. The demonstrated TEM in situ tensile bar fabrication method can thus be used to ascertain mechanical properties such as yield stress, UTS, modulus of elasticity, and elongation for materials that necessitate depth-specific examination at the nanoscale, such as ion-irradiated layers.

ACKNOWLEDGEMENTS

This research was sponsored by the National Science Foundation award DMR-17-52636 (PW) and the US Department of Energy Office of Nuclear Energy award DE-NE0008758 (GW). Portions of the microscopy effort were supported by the US DOE Office of Nuclear Energy under DOE Idaho Operations Office contract DE-AC07-05ID14517 as part of the Nuclear Science User Facilities experiment 19-1723. The authors also acknowledge Dr. Kayla Yano from Pacific Northwest National Laboratory for technical discussions and Matthew Besser at Ames Laboratory for assistance with alloy fabrication. Full TEM in situ video files and load-displacement data are permanently archived and accessible at doi:https://doi.org/10.4231/MQZZ-CN91.

REFERENCES

1. S.J. Zinkle and L.L. Snead, *Scr. Mater.* 143, 154–160 (2018).
2. G.S. Was, *J. Mater. Res.* 30, 1158–1182 (2015).
3. L. Shao, J. Gigax, D. Chen, H. Kim, F.A. Garner, J. Wang, and M.B. Toloczko, *Nucl. Instruments Methods Phys. Res. B* 409, 251–254 (2017).
4. P. Hosemann, D. Kiener, Y. Wang, and S.A. Maloy, *J. Nucl. Mater.* 425, 136–139 (2012).
5. D.E.J. Armstrong, C.D. Hardie, J. Gibson, A.J. Bushby, P.D. Edmondson, and S.G. Roberts, *J. Nucl. Mater.* 462, 374–381 (2015).
6. C.K. Dolph, D.J. da Silva, M.J. Swenson, and J.P. Wharry, *J. Nucl. Mater.* 481, 33–45 (2016).
7. H. Vo, A. Reichardt, C. Howard, M.D. Abad, D. Kaoumi, P. Chou, and P. Hosemann, *JOM* 67, 2959–2964 (2015).
8. X. Bai, S. Wu, P.K. Liaw, L. Shao, and J. Gigax, *Metals* 7, 25 (2017).
9. K.S. Mao, C. Sun, Y. Huang, C.-H. Shiau, F.A. Garner, P.D. Freyer, and J.P. Wharry, *Materialia* 5, 100208 (2019).
10. A. Kareer, A. Prasitthipayong, D. Krumwiede, D.M. Collins, P. Hosemann, and S.G. Roberts, *J. Nucl. Mater.* 498, 274–281 (2018).
11. M. Saleh, A. Xu, C. Hurt, M. Ionescu, J. Daniels, P. Munroe, L. Edwards, and D. Bhattacharyya, *Int. J. Plast.* 112, 242–256 (2019).
12. S. Özerinç, R.S. Averback, and W.P. King, *J. Nucl. Mater.* 451, 104–110 (2014).
13. P. Landau, Q. Guo, P. Hosemann, Y. Wang, and J.R. Greer, *Mater. Sci. Eng. A* 612, 316–325 (2014).
14. K.S. Mao, C. Sun, X. Liu, H.J. Qu, A.J. French, P.D. Freyer, F.A. Garner, L. Shao, and J.P. Wharry, *J. Nucl. Mater.* 528, 151878 (2020).
15. K.S. Mao, C. Sun, C.-H. Shiau, K.H. Yano, P.D. Freyer, A.A. El-Azab, F.A. Garner, A. French, L. Shao, and J.P. Wharry, *Scr. Mater.* 178, 1–6 (2020).
16. P. Hosemann, *Scr. Mater.* 143, 161–168 (2018).
17. P. Hosemann, C. Shin, and D. Kiener, *J. Mater. Res.* 30, 1231–1245 (2015).
18. D. Kiener, A.M. Minor, O. Anderoglu, Y. Wang, S.A. Maloy, and P. Hosemann, *J. Mater. Res.* 27, 2724–2736 (2012).
19. T. Ajantiwalay, H. Vo, R. Finkelstein, P. Hosemann, and A. Aitkaliyeva, *JOM* 72, 113–122 (2020).
20. D. Kiener, P.J. Guruprasad, S.M. Keralavarma, G. Dehm, and A.A. Benzerga, *Acta Mater.* 59, 3825–3840 (2011).
21. S. Mao, S. Shu, J. Zhou, R.S. Averback, and S.J. Dillon, *Acta Mater.* 82, 328–335 (2015).
22. W.-Z. Han, M.-S. Ding, and Z.-W. Shan, *Scr. Mater.* 147, 1–5 (2018).
23. C. Chisholm, *Quantitative In Situ TEM Studies of Small-Scale Plasticity in Irradiated and Unirradiated Metals*, Ph.D. Dissertation (Berkeley: University of California, 2015).
24. M.-S. Ding, L. Tian, W.-Z. Han, J. Li, E. Ma, and Z.-W. Shan, *Phys. Rev. Lett.* 117, 215501 (2016).
25. K.H. Yano, M.J. Swenson, Y. Wu, and J.P. Wharry, *J. Nucl. Mater.* 483, 107–120 (2017).
26. K.H. Yano, M.J. Swenson, and J.P. Wharry, *J. Nucl. Mater.* 502, 201 (2018).
27. G.S. Jawaharram, P.M. Price, C.M. Barr, K. Hattar, R.S. Averback, and S.J. Dillon, *Scr. Mater.* 148, 1–4 (2018).
28. H.J. Qu, K.H. Yano, P.V. Patki, M.J. Swenson, and J.P. Wharry, *J. Mater. Res.* (2020). https://doi.org/10.1557/jmr.2019.295.
29. J. Kacher, C. Kirchlechner, J. Michler, E. Polatidis, R. Schwaiger, H. Van Swygenhoven, M. Taheri, and M. Legros, *MRS Bull.* 44, 465–470 (2019).
30. E. Spiecker, S.H. Oh, Z.-W. Shan, Y. Ikuhara, and S.X. Mao, *MRS Bull.* 44, 443–449 (2019).
31. D. Kiener, P. Hosemann, S.A. Maloy, and A.M. Minor, *Nat. Mater.* 10, 608–613 (2011).
32. G. Dehm, B.N.N. Jaya, R. Raghavan, and C. Kirchlechner, *Acta Mater.* 142, 248–282 (2018).
33. P.J. Imrich, C. Kirchlechner, D. Kiener, and G. Dehm, *JOM* 67, 1704–1712 (2015).
34. J. Cumings and A. Zettl, *Science* 289, 602–604 (2000).
35. Y. Zhu and H.D. Espinosa, *Proc. Natl. Acad. Sci.* 102, 14503–14508 (2005).
36. M.A. Haque and M.T.A. Saif, *Scr. Mater.* 47, 863–867 (2002).
37. X. Wang, K. Chen, Y. Zhang, J. Wan, O.L. Warren, J. Oh, J. Li, E. Ma, and Z. Shan, *Nano Lett.* 15, 7886–7892 (2015).
38. D. Kiener and A.M. Minor, *Nano Lett.* 11, 3816–3820 (2011).
39. V. Samaeeaghmiyoni, H. Idrissi, J. Groten, R. Schwaiger, and D. Schryvers, *Micron* 94, 66–73 (2017).

40. B.M. Morrow, E.K. Cerreta, R.J. Mccabe, and C.N. Tome, *JOM* 67, 1721–1728 (2015).
41. Q. Yu, L. Qi, K. Chen, R.K. Mishra, J. Li, and A.M. Minor, *Nano Lett.* 12, 887–892 (2012).
42. L. Jiang, T. Hu, H. Yang, D. Zhang, T. Topping, E.J. Lavernia, and J.M. Schoenung, *Nanoscale* 8, 10541 (2016).
43. L.A. Giannuzzi, J.L. Drown, S.R. Brown, R.B. Irwin, and F.A. Stevie, *Microsc. Res. Tech.* 41, 285–290 (1998).
44. D. Kiener, C. Motz, M. Rester, M. Jenko, and G. Dehm, *Mater. Sci. Eng. A* 459, 262–272 (2007).
45. T. Malis, S.C. Cheng, and R.F. Egerton, *J. Electron Microsc. Tech.* 8, 193–200 (1988).
46. G. Sainath and B.K. Choudhary, *Mater. Sci. Eng. A* 640, 98–105 (2015).
47. G. Sainath and B.K. Choudhary, *Comput. Mater. Sci.* 111, 406–415 (2016).
48. C.J. Healy and G.J. Ackland, *Acta Mater.* 70, 105–112 (2014).
49. A. Ojha, H. Sehitoglu, L. Patriarca, and H.J. Maier, *Model. Simul. Mater. Sci. Eng.* 22, 1–21 (2014).
50. C. Chisholm, H. Bei, M.B. Lowry, J. Oh, S.A. Syed Asif, O.L. Warren, Z.W. Shan, E.P. George, and A.M. Minor, *Acta Mater.* 60, 2258–2264 (2012).
51. H. Yilmaz, C.J. Williams, J. Risan, and B. Derby, *Materialia* 7, 100424 (2019).
52. A.S. Schneider, B.G. Clark, C.P. Frick, P.A. Gruber, and E. Arzt, *Philos. Mag. Lett.* 90, 841–849 (2010).
53. E. Arzt, *Acta Mater.* 46, 5611–5626 (1998).
54. J.R. Greer and J.T.M. De Hosson, *Prog. Mater Sci.* 56, 654–724 (2011).
55. J.P. Wharry, K.H. Yano, and P.V. Patki, *Scr. Mater.* 162, 63–67 (2019).
56. D. Kiener, W. Grosinger, G. Dehm, and R. Pippan, *Acta Mater.* 56, 580–592 (2008).
57. J.D. Nowak, A.R. Beaber, O. Ugurlu, S.L. Girshick, and W.W. Gerberich, *Scr. Mater.* 62, 819–822 (2010).
58. A.H.W. Ngan, X.X. Chen, P.S.S. Leung, R. Gu, and K.F. Gan, *MRS Commun.* 7, 131–140 (2017).
59. T.A. Parthasarathy, S.I. Rao, D.M. Dimiduk, M.D. Uchic, and D.R. Trinkle, *Scr. Mater.* 56, 313–316 (2007).
60. V. Samaee, R. Gatti, B. Devincre, T. Pardoen, D. Schryvers, and H. Idrissi, *Sci. Rep.* 8, 1–11 (2018).
61. M.D. Uchic, D.M. Dimiduk, J.N. Florando, and W.D. Nix, *Science* 305, 986–989 (2004).
62. C.A. Volkert and E.T. Lilleodden, *Philos. Mag.* 86, 5567–5579 (2006).
63. S.H. Oh, M. Legros, D. Kiener, and G. Dehm, *Nat. Mater.* 8, 95–100 (2009).
64. H. Tang, K.W. Schwarz, and H.D. Espinosa, *Acta Mater.* 55, 1607–1616 (2007).
65. W.D. Nix, J.R. Greer, G. Feng, and E.T. Lilleodden, *Thin Solid Films* 515, 3152–3157 (2007).
66. H. Liang, M. Upmanyu, and H. Huang, *Phys. Rev. B* 71, 241403 (2005).
67. F.F. Csikor, C. Motz, D. Weygand, M. Zaiser, and S. Zapperi, *Science* 318, 251–254 (2007).
68. W.D. Callister and D.G. Rethwisch, *Materials Science and Engineering*, 9th ed. (New York: Wiley, 2014).